

# Ultrafast phonon dynamics at the 2D limit: a comparison of time- and momentum-resolved electron scattering to *ab initio* calculations

Preliminary Exam Report

Tristan Britt (260898980)

10<sup>th</sup> June 2022

Submitted in partial fulfillment of the requirements  
for the degree of Doctor of Philosophy

to the

Department of Physics  
at McGill University

Exam Committee Chair  
1st Reviewer  
2nd Reviewer  
3rd Reviewer

Prof. Dr. Jonathan Sievers  
Prof. Dr. Bradley J Siwick  
Prof. Dr. Patnajali Kambhapathi  
Prof. Dr. Nikolas Provatas

# Contents

---

CONTENTS	ii
1 TWO-DIMENSIONAL MATERIALS	1
1.1 Reduced dimensionality . . . . .	1
1.2 Applications . . . . .	2
1.3 Manufacturing 2D materials . . . . .	3
2 METHODOLOGY	5
2.1 Dynamics . . . . .	6
2.2 <i>Ab-initio</i> ultrafast electron diffraction . . . . .	7
2.2.1 Time-dependent Boltzmann equation . . . . .	7
2.2.1.1 Solving the TDBE . . . . .	9
2.2.2 Computing dynamic structure factor and phonon-induced scattering intensity . . . . .	9
3 PROPOSAL	10
3.1 Dissertation breakdown . . . . .	10
3.1.1 Chapter 1: 1L-MoS <sub>2</sub> with linearly polarised photoexcitation . . . . .	10
3.1.2 Chapter 2: 1L-MoS <sub>2</sub> with circularly polarised photoexcitation . . . . .	10
3.1.2.1 Selection rules for $\sigma^\pm$ photoexcitation in 1L-MoS <sub>2</sub> . . . . .	10
3.1.2.2 Observation of chiral phonons from ultrafast electron diffuse spectroscopy . . . . .	12
3.1.3 Chapter 3: Thermoelectric SnSe . . . . .	13
3.2 Timeline . . . . .	13
3.2.1 Additional experiments . . . . .	14
A ONE PHONON STRUCTURE FACTOR	15
B COLLISION INTEGRALS OF THE TDBE	16
BIBLIOGRAPHY	18

# 1

## Two-Dimensional Materials

---

The history of material science is a continually evolving story, dating back to antiquity. It is so central to the understanding of the development of the modern age that the critical epochs in history are named after the advances in materials during that time (the Stone age, Bronze age, the Iron age, the Golden<sup>1</sup> age, etc.). For most of modern scientific history, the choice of material for a given application was limited solely to its composition, what atoms constituted the solid. However, with the advent and subsequent development of condensed matter physics, experimentalists have begun to probe materials for an ever increasing variety of reasons: how readily electrons drift through the material when an electric field is applied, how tightly atoms are bound together, how willing a material is to ionize, etc. Most critically, we have also begun to consider a final aspect of materials: their size.

### 1.1 REDUCED DIMENSIONALITY

Obviously existing in three spatial dimensions, most materials and their properties are dependent on each of these dimensions. However, we can create and quantify other systems where the physical size and/or material properties are functions of a reduced number of dimensions. By removing one spatial dimension, we can convert a bulk (3D) material into a two dimensional (2D) material. The first example of an isolated 2D material was graphene, a perfectly hexagonal arrangement of carbon atoms, in 2004 [1]. Since then, many other bulk systems have had nanosheets synthesized from them [2]. We can further reduce the dimensionality and create nanotubes (nanowires) that only have material properties varying along a single spatial dimension (1D). In the most extreme case, we can create nanometer-scale semiconductor particles quantum confined in colloidal suspensions that behave as zero-dimensional (0D) systems called *quantum dots*, first theorized in 1982, and first realised by Louis Brus in 1983 [3].

While nanotubes and quantum dots have experimentally promising industrial applications, 2D materials have yet to be fully taken advantage of, as the material properties of strictly two dimensions have been complicated to untangle and thus exploit. Whilst many atomic configurations of bulk materials can yield 2D sheets [4, 5, 6], 2D transition metal dichalcogenides (TMDs) are currently the subject of intense research. These are materials whose atomic configuration is  $MX_2$ , where  $M$  is a transition metal, and  $X$  is a chalcogenide. In bulk, these materials have an indirect band gap transition, but in the monolayer (1L), the transition is direct and in the visible range, yielding exciting electronic and optoelectronic properties.

In general, there are a few key properties of 2D materials that have motivated their exploration.

#### ► VAN DER WAALS INTERACTIONS

Bulk TMDs are known as *van der Waals* (*vdW*) materials, 2D layers that are weakly bound together by van der Waals interactions. In the bulk, these weak interactions cause low tensile strength owing to the little force required to break these structural bonds. Conversely in the monolayer, only strong covalent bonds are present, making the

---

<sup>1</sup>This is the familial name for the age of modern computing.

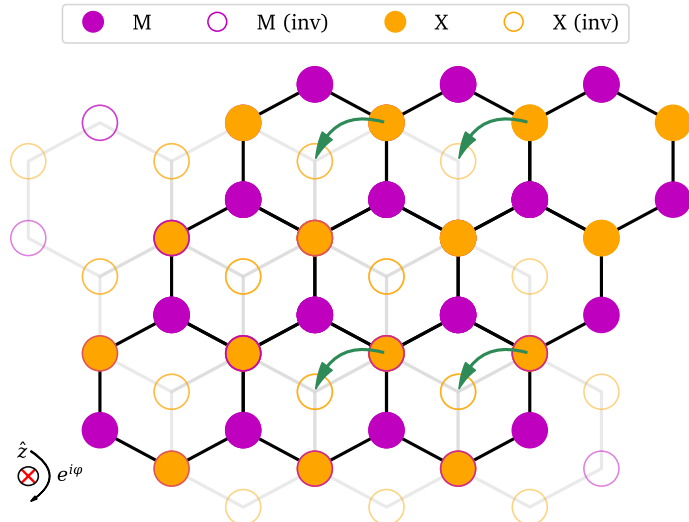


FIGURE 1.1: Broken spatial inversion symmetry in hexagonal 2D TMD ( $\text{MX}_2$ ) lattices. Inversion about the unit cell center (the transition metal) by the standard  $C_3^+$  of the  $D_{3h}$  symmetry of creates an incommensurate lattice that yields (quasi)particles with potentially nonzero orbital and spin azimuthal and magnetic quantum numbers.

engineering of 2D Coulomb materials more promising than that of a materials' bulk counterpart. The breaking of vdW forces in graphite means, for example, that graphene has  $> 1000\times$  greater tensile strength than graphite [7].

► SURFACE AREA-TO-VOLUME RATIO

Owing to the increased surface area of 2D materials, they are much more susceptible to environmental conditions than their bulk counterparts. Thermal transport, electron-lattice coupling, and many other properties are readily influenced by changes in dielectric environment, external electric fields, and others [8] (cite your work).

► IN-PLANE CONFINEMENT

In addition to the creation of a visible-range direct bandgap transition, the transformation from bulk to monolayer in TMDs also creates more strongly-bound excitons, due to the increased Coulomb interaction from the reduction of electron-hole screening [9]. Both of these properties can be attributed to the lack of spatial inversion symmetry (see Figure 1.1) the monolayer exhibits compared to the bulk [10], and can be tuned depending on the number of layers present in the sample. Furthermore, combinations of monolayers into heterostructures can create exotic optical, electronic, and vibrational properties not found in the constituent materials, such as Moiré excitons [11].

## 1.2 APPLICATIONS

► PHOTOVOLTAICS

Most TMDs, black phosphorous<sup>2</sup>, and other 2D materials have bandgaps in the visible to near infrared with impressive absorption capabilities such as absorbing as much light in 1 layer of TMD as 100nm of silicon [12]. While insufficient to replace tradition high-efficiency photovoltaics, modifications into heterostructures have allowed monolayer TMDs to achieve as high as  $10^8 \text{ A/W}$  of optical sensitivity [13, 14]. Furthermore, since the bandgap and work function of these materials can be tuned [9], 2D TMDs find applications as the electron

<sup>2</sup>This layered arrangement of phosphorus atoms creates a puckered 2D structure that can be cleaved from its vdW bulk configuration, where the principle axes are often referred to as the "zigzag" and "armchair" directions.

transporting layer (ETL) or hole transporting layer (HTL) for organic and perovskite solar cells [15]. Whilst promising tunable electronic properties of 2D materials have been put forth, there is much reconciliation to be done between the 2D materials community and the conventional solar cell community, such as the tradeoff between the increase in conductivity of graphene ETLs/HTLs with the number of layers and the corresponding reduction in transparency that is needed for low series and shunt resistances (and thus efficient solar cells) [16].

#### ► ARTIFICIAL HETEROSTRUCTURES

With the advent of monolayer materials, we can stack various layers of potentially contrasting materials to create artificially hetero-structured vdW materials that exhibit exotic properties. By stacking two sheets of graphene at specific twist angles (relative to the local hexagonal symmetry), researchers have been able to find 'magic angles' such that the heterostructure is insulating (blocking all electron flow), or exhibits unconventional superconductivity [17]. Phononic mechanisms in such systems can also be tunably renormalised by varying the same twist angle [18]. Furthermore, electronic band structures, inter-layer excitons, resulting charge carrier scattering mechanisms, and more can be arbitrarily tuned in such systems [19, 20, 21].

#### ► VALLEY- AND SPINTRONICS

These (opto)electronic properties arise from the highly correlated nature of TMD's spin [22, 23], valley [24, 25], electronic [26], and vibrational [27] degrees of freedom which can vary dramatically with the number of layers, most notably with the breaking of inversion symmetry in monolayers. In 1L-MoS<sub>2</sub>, strong spin-orbit coupling additionally [28] allows for direct control of the spin and valley degrees of freedom [10, 24] and the possibility of exciting chiral phonons [29, 30]. The coupling of monolayers in heterostructures [31], moiré superlattices [11, 32] or to underlying substrates [33] and modified dielectric environments [34] have opened further avenues for wide tunability in properties and control of these correlated phases.

Many effects in these (and other) 2D materials arise specifically from the interplay between electronic and vibrational degrees of freedom, known as electron-phonon coupling (EPC) [35]. EPC is a central concern in materials physics generally, providing the fundamental origin of phenomena as diverse as conventional superconductivity [36], charge-density waves [37] and soft-mode phase transitions [38], and playing an important role in determining both charge and thermal transport properties. However, unlike their 3D counterparts where EPC is a fundamental property of the materials, EPC should be uniquely sensitive to the environment of a 2D material where the Coulomb potential is known to be poorly screened within the 2D layer [39]. It is this EPC that drives the unique properties of monolayers, and is the focus of most TMD research. Experiments probing the electronic state of TMD monolayers have been developed most, from time-resolved angle-resolved photoemission spectroscopy (trARPES) of the bandgap renormalization in 1L-MoS<sub>2</sub>[9], to magnetophotoluminescence measurements of exciton and trion formation [40], and others. There have been less efforts aimed at probing the vibrational system, as the means to do so reliable have been lacking.

**!** The proposal herein aims to examine the time-resolved dynamics of the phononic system of TMD monolayers at all momenta in the Brillouin zone (BZ), and systematically determine its role in the unique properties exhibited by the monolayers.

### 1.3 MANUFACTURING 2D MATERIALS

2D materials can be manufactured in two qualitatively different methods.

► SUBTRACTIVE

These methods rely on mechanical exfoliation, also known as the "scotch tape method". It relies on exploiting the weak interlayer vdW forces in bulk materials. Adhesion of the tape surface to the surface of the bulk involves forces greater than the vdW interaction, and by mechanically separating the two surfaces, a monolayer is removed from the bulk crystal and remains adhered to the tape. Erosion of the tape then leads to deposition of the monolayer onto various substrates for use in transmission electron microscopy (TEM) and ultrafast electron diffraction (UED) experiments [41]. Samples can also be subtractively manufactured by liquid exfoliation. In this method, the operating principle is the same, except that the mechanical force required to separate the layers is applied via an organic solvent surrounding the bulk material. Sonication induces interlayer tensile stress, causing separation. The drawback of this method is low monolayer yield, small sample size, and often high defect densities and residual solvent, making deposition and subsequent use in transmission UED experiments difficult, if not impossible. Improvements to the sonication method have recently yielded improved sample quality, making liquid exfoliation a potential avenue forward for consistent sample generation [42].

► ADDITIVE

By contrast, we can generate monolayers "manually" by building up the monolayer from the constituent atomic ingredients. Chemical vapour deposition (CVD) relies on the reaction of heated precursor gases (containing the necessary atoms) with the substrate in a furnace, condensing and forming thin layers of the material. Many parameters will impact the physical qualities of the sample, and such makes this process more complex and expensive than the methods mentioned previously. Its advantage, however, is its large scalability once the recipe for efficient, stable generation of monolayers has been achieved [43].

# 2

## Methodology

---

Materials are constituted of arrangements of atoms. The structure of materials is crucial in understanding the macro- and microscopic behaviour of the relevant degrees of freedom. Diffraction has been the most common tool used historically to probe the structure of matter, examining structure from  $10^{-8}$  -  $10^{-4}$  cm in magnitude. The earliest recorded crystallographic example concerning the arrangement of atoms in a material was with the hexagonal symmetry of snowflake crystals by Johannes Kepler in his 1611 work *A New Year's Gift of Hexagonal Snow* [44]. At the time of his examination, however, there was not yet an ability to probe materials on the microscopic scales needed to "paint a whole picture" of the material. It was not until Max von Laue's 1912 observation [45] of the interference patterns in diffracted x-rays that condensed matter experimentalists had a tool to examine crystal structure.

The most relevant advance in diffraction technology since its inception is the development of electron diffraction. Experimentally realised by Clinton Joseph Davisson and George Paget Thomson separately in 1927 [46, 47], electron diffraction provides many benefits to diffraction crystallography. In this method, the charge of the incident electron interacts with the nuclear charge screened by the surrounding electrons, generating an outgoing electron wavefunction. Unlike x-ray diffraction, the Ewald sphere for 100 keV electrons is much more flat<sup>1</sup>, meaning that a single electron detector can record meaningful data over the same range of angles as multiple x-ray detectors. Furthermore, owing to the  $> 10^5$  increase in scattering cross-section than x-rays [48], electron scattering does not suffer as much from the reduction in diffraction intensity at high scattering angles due to the atomic form factor of the atoms in the material, despite the electron atomic form factor decreasing more quickly with momentum than their x-ray equivalent. This allows electrons to diffract strongly off the atoms in the crystal. Electron sources are also cheaper, and physically less demanding than high-energy x-ray or neutron sources, making them more accessible to a larger range of experimentalists.

The primary historic motivation to use (electron) diffraction was for the recreation of the real-space atomic positions in the lattice, owing to the fact that the diffraction intensity of the elastic scattering events collected in transmission is related to the Fourier transform of the interatomic lattice potential (which follows the same periodicity as the nuclear sites in the lattice). At finite temperature, the atoms will have increased thermal energy, and will have nonzero displacements from their positions in thermal equilibrium. We can understand this atomic motion by approximating it as a linear combination of independent harmonic oscillators in what is now known as the 'normal mode coordinate formalism', and create a reciprocal-space picture of propagating lattice waves called *phonons*. In this formalism, we can expand the diffracted intensity as an infinite sum of terms representing higher order scattering processes (with correspondingly decreasing cross-sections), namely:

$$I_{\text{all}}(\mathbf{Q}) = I_0(\mathbf{Q}) + I_1(\mathbf{Q}) + \dots \quad (2.1)$$

---

<sup>1</sup>This is quantified in the de Broglie wavelengths of 100 keV electrons ( $\sim 0.037$  Å) versus hard x-ray wavelengths ( $\sim 0.2$  nm), meaning that 100 keV have wavelengths smaller than the average atomic spacing and are thus capable of observing physics with higher resolution.

We can write the transmitted diffraction intensity from elastic scattering  $I_0$ , known as the 'Bragg' intensity, as:

$$I_0(\mathbf{Q}) = \frac{N_c^2 m_e^2}{4\pi^2 \hbar^4 r^2} \left| \sum_{\{\mathbf{H}\}} \sum_c^{\# \text{cells}} \sum_{\kappa}^{\# \text{atoms}} f_{\kappa}(\mathbf{Q}) e^{-W_{\kappa}(\mathbf{Q}; T)} e^{-i\mathbf{Q} \cdot (\mathbf{R}_c + \boldsymbol{\tau}_{\kappa})} \delta(\mathbf{Q} - \mathbf{H}) \right|^2 \quad (2.2)$$

where  $N_c$  is the number of unit cells in the crystal,  $f_{\kappa}$  is the electron atomic form factor<sup>2</sup>,  $\mathbf{R}_c$  is the displacement to the  $c^{\text{th}}$  unit cell,  $\boldsymbol{\tau}_{\kappa}$  is the location of the  $\kappa^{\text{th}}$  atom with respect to the unit cell origin,  $\mathbf{Q}$  is the scattering vector, enumerating the angle by which the scattering electron is deflected in the scattering event, and  $\mathbf{H}$  are the locations of the Bragg peaks<sup>3</sup>. The most important term in this expression is  $W_{\kappa}(\mathbf{Q}; T)$ , known as the *Debye-Waller factor*. This is the term that directly describes the suppression of Bragg peak intensity that can be shown to be related to the atomic mean-squared displacement (MSD) via  $e^{-W_{\kappa}} \sim e^{-\langle u_{\kappa}^2 \rangle}$  [49].

Yet at finite temperature, the statistical likelihood of inelastic scattering events between the electron and the positively-charged nuclear cores increases, and the resulting diffraction pattern will include more information than simply the elastic 'Bragg' scattering. The resulting inelastic diffuse scattering  $I_1$  can be written as:

$$I_1(\mathbf{Q}) = \frac{N_c m_e^2}{r^2 \hbar^3} \sum_{\nu} \frac{n_{\mathbf{q}\nu} + 1/2}{\omega_{\mathbf{q}\nu}} |F_{1\nu}(\mathbf{Q}; \{\mathbf{e}_{\mathbf{q}\nu}\})|^2 \quad (2.3)$$

where  $\mathbf{q}$  is the reduced scattering vector describing the momentum of a phonon inside a given Brillouin zone<sup>4</sup>,  $n$  describes the occupation of a phonon branch  $\nu$  at momentum  $\mathbf{q}$ ,  $\hbar\omega$  is the energy of such a mode, and  $|F_{1\nu}|^2$  is a geometrical factor describing the coupling strength of a given mode to scattering electrons as the *one-phonon structure factor*. It is inherently dependent on the set of atomic displacements created by the phonons  $\{\mathbf{e}_{\mathbf{q}\nu}\}$ , and includes the Debye-Waller term seen in Eq. (2.2) (see Appendix A). Note that higher order scattering events can be successively represented as  $I_2$ ,  $I_3$ , etc., but they have scattering cross sections orders-of-magnitude smaller than the diffuse intensity in the systems of interest herein [50, 51] and as such do not represent experimentally accessible quantities. The key factor here is the linear dependency on the phonon occupations. As phonons are occupied across the lattice, the resulting occupation can be directly tracked with the corresponding changes in diffuse intensity (between the Bragg peaks) by interrogation of the transmitted diffraction pattern at the appropriate  $\mathbf{Q}$  points.

## 2.1 DYNAMICS

In these experiments, we focus on 2 main goals.

- STRUCTURAL CHANGES

The advantage of UED is that it allows us to study materials far from equilibrium. Following the application of the external perturbations due to pulses of light, we can follow how the structure changes. The change in crystal structure is reflected in the time dependence of  $I_0$ . As the infrastructure to generate ultrafast pulses of light has been well developed with the advent of chirped pulse amplifiers and x-ray free electron lasers (XFELs), the creation of ultrafast photoexcitation pulses and ultrafast x-ray pulses is a well solved problem. The ability to create pulses of neutrons, however, has not been well developed, and the spacecharge problem of electron bunches initially posed a challenge in creating ultrafast electron bunches. The use of a radiofrequency (RF) compressor, in combination with stabilisation electronics [52], have paved the way for reliable generation of

<sup>2</sup>This describes the electron 'cloud' around a given atom, and is the Fourier transform of the real-space atomic charge density.

<sup>3</sup>These are the locations in  $\mathbf{k}$ -space of the Fourier transforms of the atomic positions. The  $\delta$  function in Eq. (2.2) is a representation of the *Laue condition*, which says that there will only be appreciable elastic scattering at these Bragg peaks. The actual measured signal will be a convolution of the sample response with a function describing the spatial resolution of the instrumentation, in practice relaxing this  $\delta$  function constraint, yielding Bragg diffraction for a range of  $\mathbf{Q}$  centered around  $\mathbf{H}$ .

<sup>4</sup>The reduced wavevector is sometimes known as the *deviation vector*  $\mathbf{s}$  in conventional TEM literature.

stable ultrafast electron imaging bunches for use in a time-resolved UED experiment, allowing resolution of lattice dynamics happening as quickly as 100 fs.

► EPC

The stabilisation infrastructure mentioned above has in recent years allowed for the development of ultrafast electron diffuse spectroscopy (UEDS), which allows for direct observations of electron-lattice coupling by perturbing the electron system and watching how the subsequent excitation (relaxation) dynamics couple to the phononic system. This local phonon enhancement is observed through the dynamic evolution of  $I_1$ . This electron analog of x-ray diffuse scattering has previously provided momentum-resolved information on inelastic electron-phonon scattering [53, 54, 55, 56], soft phonon physics [37], and polaron formation [57] in bulk materials.

We make the connection between lattice dynamics and the Bragg and diffuse intensities via the Debye-Waller term and phonon occupations. As mentioned, the Debye-Waller term is directly proportional to the MSD  $\langle u^2 \rangle$ , so as the solid undergoes a reversible process, the change in Bragg peak intensity will inform on increases in the atomic MSD. The diffuse intensity can contemporaneously give insight to the instantaneous local phonon enhancement via the phonon occupations  $n_{q\nu}$ . In this way, the diffraction intensity can yield a direct view of the lattice dynamics in a given material.

In the pump-probe scheme, photoexcitation on the sample will excite charge carriers throughout the electronic band structure. After a fixed time delay  $\tau$ , an imaging bunch of scatterers will be deflected by the lattice via Coulomb repulsion with the positive cores and charge carrier density. The electrons in the material will then thermalize amongst themselves via electron-electron scattering, and be reasonably well described by a Fermi-Dirac distribution at an elevated temperature. From here, the electrons will relax back to the Fermi level by interacting with the lattice. The subsequent thermal motion of the atoms within the lattice is determined via the changes in Bragg intensity, and the lattice relaxation dynamics are inferred from changes in the diffuse. By taking repeat images, recording (in)elastic collision events in transmission, for varying time delays, we can recreate a stroboscopic movie of the lattice dynamics observed. The use of ultrafast electron bunches and ultrafast laser pulses allow time resolution in such an experiment to be limited to <100 fs, allowing for precise determination of the dynamics of various physical processes. A schematic of the UEDS instrument capable of observing time-resolved dynamics is given in [Figure 2.1](#).

## 2.2 ab-initio ULTRAFAST ELECTRON DIFFRACTION

The advent of first-principles theory and evolving advances in computational techniques now allow for the direct simulation of various physical processes, to confirm or reject observations and further motivate research. It was not until recently [50, 51] that researchers had the ability to simulate, from first-principles, an ultrafast electron diffraction experiment. We briefly peruse the computational framework that we plan to use to support the experiments proposed in [Chapter 3](#).

### 2.2.1 Time-dependent Boltzmann equation

The time dependence of the electronic and vibrational occupations can be modelled via the time-dependent Boltzmann equation (TDBE) [58]. In this scheme, initial temperatures of each degree of freedom,  $T_0^{\text{el}}$  and  $T_0^{\text{ph}}$  respectively, are used to initialise the electron and phonon occupancies,  $f_{nk}$  and  $n_{q\nu}$ , to the Fermi-Dirac and Bose-Einstein distributions. Propagating the system according to [Eq. \(2.4\)](#) allows direct determination of these occupations with arbitrary time and momentum resolution.

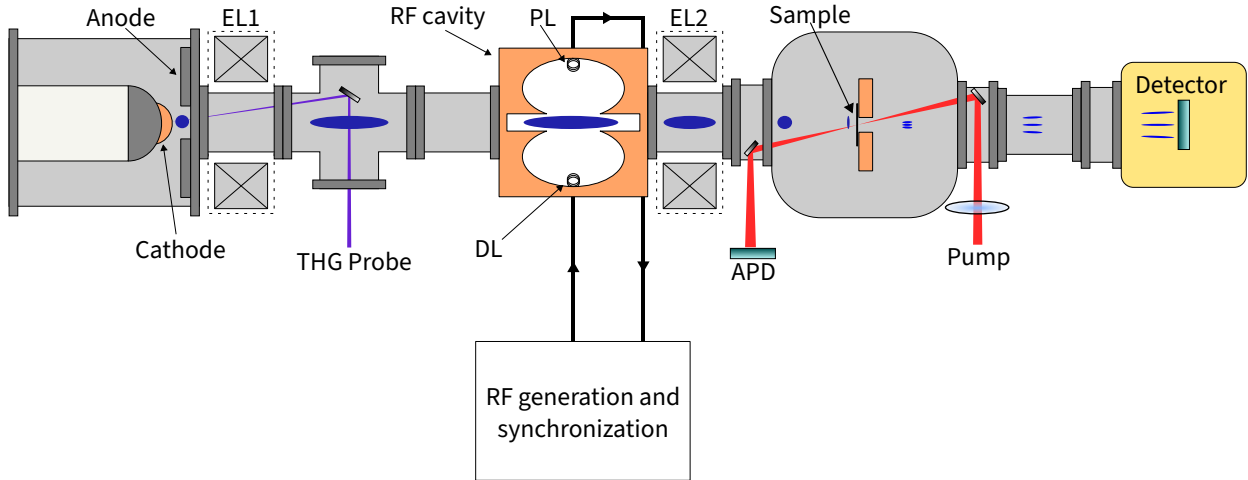


FIGURE 2.1: Schematic of the UEDS beamline at McGill, to be viewed from left to right. Ultrafast UV light generates emission off a bulk copper photocathode. After spatial and temporal focusing, the slightly-convergent electron pulse train diffracts off the sample, and is subsequently imaged onto the detector. By adjusting the time delay between the electron pulse train arrival time and the pump train arrival time, we obtain time-resolved diffraction patterns.

$$\frac{\partial f_{nk}}{\partial \tau} = \Gamma_{nk}^{e-ph}(f_{nk}, n_{q\nu}; \tau) \quad (2.4a)$$

$$\frac{\partial n_{q\nu}}{\partial \tau} = \Gamma_{q\nu}^{ph-e}(n_{q\nu}, f_{nk}; \tau) + \Gamma_{q\nu}^{ph-ph}(n_{q\nu}; \tau) \quad (2.4b)$$

Here,  $\Gamma^{x-y}(\tau)$  are the collision integrals used to describe the scattering rates of emissive and coalescing processes in and between the electronic and vibrational systems<sup>5</sup> for a propagation time  $\tau$ . Including the phonon-phonon interactions explicitly takes into account the available phase space for anharmonic three-phonon processes, while the phonon-electron term describes the transfer of energy to the lattice from the excited carriers relaxing to the Fermi level. It is important to note that the electron-phonon and phonon-electron collision integrals directly depend on the amplitude of the  $e\text{-}ph$  coupling matrix elements, namely  $|g_{mn\nu}(\mathbf{k}, \mathbf{q})|^2$ , where  $m, n$  index the Kohn-Sham electronic eigenstates, and  $\mathbf{k}$  is the electron momentum.

At thermal equilibrium ( $T_0^{\text{el}} = T_0^{\text{ph}}$ ), the system is stable, and each population will remain constant. However, as  $T_0^{\text{el}} > T_0^{\text{ph}}$ , electron-phonon interactions will start to drive the system back to equilibrium. Such a condition is created in the UEDS experiment, and so both approaches are suited to probe the dynamics of EPC-induced effects. We extract the dynamic lattice "temperature"<sup>6</sup> from the phonon occupations of the TDDE by inverting the Bose-Einstein distribution:

$$T_{q\nu}(\tau) = \hbar \omega_{q\nu} \{k_B \ln[1 + n_{q\nu}(\tau)]\}^{-1} \quad (2.5)$$

Newfound techniques of Zacharias *et al* [50, 51] can be used for inexpensive computation of the diffraction intensity to all orders. The total scattering intensity  $I(\mathbf{Q}; T)$  for a given lattice temperature  $T$  can be evaluated using the Laval-Born-James (LBJ) theory [59, 60, 61]. Iteratively evaluating the LBJ formula for the simulated TDDE temperature at a given time delay yields time-resolved diffuse scattering intensities resulting from all scatterers of the probing electron bunch. These sequential simulations in turn allow direct comparison of the UEDS measurements to first principles results.

<sup>5</sup>Electron-electron scattering is not expected to contribute in the physical or virtual system, as the electron occupation at each step can be reasonably described by a Fermi-Dirac distribution [58].

<sup>6</sup>While the assignment of  $T_{q\nu}$  as a temperature in the thermodynamic sense is tenuous in these ultrafast regimes, it nevertheless serves as a lens through which we can understand the dynamics of the lattice.

### 2.2.1.1 Solving the TDBE

In order to solve the coupled Eq. (2.4), we start by specifying initial conditions for the electron and phonon occupations, satisfying Fermi-Dirac and Bose-Einstein statistics respectively.

$$f_{n\mathbf{k}}^0(\mu, T_{\text{el}}^0) = [e^{(\varepsilon_{n\mathbf{k}} - \mu)/k_B T_{\text{el}}^0} + 1]^{-1} \quad (2.6a)$$

$$n_{q\nu}^0(T_{\text{ph}}^0) = [e^{\hbar\omega_{q\nu}/k_B T_{\text{ph}}^0} - 1]^{-1} \quad (2.6b)$$

where  $T_{\text{el}}^0$  and  $T_{\text{ph}}^0$  denote the initial electronic and vibrational temperature respectively. The chemical potential  $\mu$  is solved self-consistently by the following relation for a given carrier concentration:

$$n_0 = \frac{1}{\Omega_{\text{BZ}}} \sum_m^{\text{cond}} \int d\mathbf{k} f_{m\mathbf{k}}^0(\mu, T_{\text{el}}^0) \quad (2.7)$$

where  $\Omega_{\text{BZ}}$  is the area of the two-dimensional Brillouin zone,  $n_0$  is the concentration of photo-excited carriers, and the sum extends over the conduction manifold<sup>7</sup>. The TDBE is then propagated by explicitly computing the electron-phonon and phonon-electron collision integrals, whereas phonon-phonon scattering is accounted for in the relaxation time approximation [62]. In the systems studied here, radiative carrier recombination occurs on time scales longer than 1 ns [63, 64], and as such are ignored here, as well as excitonic interactions. Euler time stepping is used with a time step of 0.5 fs. This gives the ultrafast dynamics of the electron and phonon occupations, and inverting Eq. (2.6b) allows us to extract the time-, mode-, and momentum-resolved temperature.

### 2.2.2 Computing dynamic structure factor and phonon-induced scattering intensity

Now armed with  $n_{q\nu}(\tau)$ , we can begin to compute the dynamical structure factor. Using the LBJ theory, it can be shown [51] that the phonon-induced scattering intensity that results from all phonon scattering processes for a temperature  $T$  can be written as:

$$I_{\text{all}}(\mathbf{Q}, T) = N_c \sum_c \sum_{\kappa\kappa'} f_\kappa(\mathbf{Q}) f_{\kappa'}^*(\mathbf{Q}) e^{i\mathbf{Q}\cdot[\mathbf{R}_c + \tau_\kappa - \tau_{\kappa'}]} e^{-W_\kappa(\mathbf{Q}, T)} e^{-W_{\kappa'}(\mathbf{Q}, T)} e^{P_{c,\kappa\kappa'}(\mathbf{Q}, T)} \quad (2.8)$$

The exponent of the Debye-Waller factor is defined as:

$$-W_\kappa(\mathbf{Q}, T) = -\frac{M_0}{N_c M_\kappa} \sum_{\mathbf{q} \in \mathcal{B}, \nu} |\mathbf{Q} \cdot \mathbf{e}_{\kappa, \nu}(\mathbf{q})|^2 u_{\mathbf{q}\nu}^2 - \frac{M_0}{2N_c M_\kappa} \sum_{\mathbf{q} \in \mathcal{A}, \nu} |\mathbf{Q} \cdot \mathbf{e}_{\kappa, \nu}(\mathbf{q})|^2 u_{\mathbf{q}\nu}^2 \quad (2.9)$$

where  $u_{\mathbf{q}\nu}^2 = \frac{\hbar}{2M_0\omega_{\mathbf{q}\nu}}[2n_{\mathbf{q}\nu} + 1]$  is the mode-resolved mean-squared displacement of the mode  $\nu$ , and  $\mathcal{A}$  ( $\mathcal{B}$ ) denote the sets of phonons that are (not) related by time-inversion. The exponent of the phononic factor is defined as:

$$P_{c,\kappa\kappa'}(\mathbf{Q}, T) = \frac{2M_0 N_c^{-1}}{\sqrt{M_\kappa M_{\kappa'}}} \sum_{\mathbf{q} \in \mathcal{B}, \nu} u_{\mathbf{q}\nu}^2 \mathcal{R}\{\mathbf{Q} \cdot \mathbf{e}_{\kappa, \nu}(\mathbf{q}) \mathbf{Q} \cdot \mathbf{e}_{\kappa' \nu}^*(\mathbf{q}) e^{i\mathbf{q} \cdot \mathbf{R}_c}\} + \frac{M_0 N_c^{-1}}{\sqrt{M_\kappa M_{\kappa'}}} \sum_{\mathbf{q} \in \mathcal{A}, \nu} u_{\mathbf{q}\nu}^2 \mathbf{Q} \cdot \mathbf{e}_{\kappa, \nu}(\mathbf{q}) \mathbf{Q} \cdot \mathbf{e}_{\kappa' \nu}(\mathbf{q}) \cos(\mathbf{q} \cdot \mathbf{R}_c) \quad (2.10)$$

We recover the formulae for Bragg scattering (Eq. (2.2)), one-phonon diffuse (Eq. (2.3)), and multi-phonon contributions to the scattering intensity by the corresponding first-order, second-order, and all higher order terms of the Taylor expansion of the phononic factor<sup>8</sup>. By supplying the time- and momentum-resolved temperatures computed with the TDBE, we can now determine  $I(\mathbf{Q}, \tau)$ , and provide direct comparison with experimental signals.

<sup>7</sup>This formula is readily extended to hole concentrations, with the sum going over the valence manifold instead.

<sup>8</sup>It should be noted that the fine grids of these calculations are computationally inexpensive since they do not involve extra ab-initio steps, and so these calculations act as a post-processing step. The expense is in computing the interatomic force constants, where the method of generation is not constrained in this framework.

# 3

## *Proposal*

---

The primary focus of this proposal, to be clear, is to directly compare the UEDS signals obtained and the record of phonon dynamics therein to a novel first-principles framework that replicates the dynamics of these same processes observed. We must first validate the framework by providing comparison between a typical pump-probe experiment and the *ab-initio* framework.

### 3.1 DISSERTATION BREAKDOWN

First and foremost, UEDS has not to date been performed on monolayer samples, as the means to do so with low signal-to-noise (SNR) have been lacking. The primary concern is that the Bragg intensity  $I_0 \propto N_c^2$ , while the diffuse intensity  $I_1$  is several orders of magnitude weaker, being only linear in  $N_c$ . Furthermore, being that the monolayer is mounted on a  $\text{Si}_3\text{N}_4$  substrate, an effective semi-infinite dielectric slab, only  $\sim 3\%$  of the incident electron beam will scatter from the single-crystal itself. Combined, this makes the ability to measure UEDS signals on monolayers nontrivial at best. However, after having proven that such experiments are possible, we begin by pumping with linearly polarised light.

#### 3.1.1 *Chapter 1: 1L-MoS<sub>2</sub> with linearly polarised photoexcitation*

Linear polarised light is a linear superposition of left- and right-handed light,  $|\mathbf{h}\rangle = (|l\rangle + |r\rangle)/\sqrt{2}$ , and so according to the excitation scheme in [Section 3.1.2.1](#), we will excite carriers isotropically into the system at momentum  $K + K' = K - K = \Gamma$ . The subsequent relaxation dynamics will be recorded and compared to the *ab-initio* results, see [Figure 3.1](#). This experiment has already been performed, and has been published under (insert publication info here).

#### 3.1.2 *Chapter 2: 1L-MoS<sub>2</sub> with circularly polarised photoexcitation*

We now plan to perform the same experiment except now photodoping carriers specifically at  $K$  ( $K'$ ) via  $\sigma^\pm$  photoexcitation.

##### 3.1.2.1 *Selection rules for $\sigma^\pm$ photoexcitation in 1L-MoS<sub>2</sub>*

By approximating the spin-orbit coupling by the intra-atomic contribution  $\mathbf{L} \cdot \mathbf{S}$ , we can write the total Hamiltonian of the system at the valleys as:

$$\hat{H} = at(\zeta k_x \hat{\sigma}_x + k_y \hat{\sigma}_y) + \frac{\Delta}{2} \hat{\sigma}_z - \lambda \zeta \frac{\hat{\sigma}_z - 1}{2} \hat{s}_z \quad (3.1)$$

where  $a$  is the lattice constant,  $\zeta = \pm 1$  is the index of the  $K$  ( $K'$ ) valley,  $t$  the effective hopping integral,  $\Delta$  the Kohn-Sham direct band gap,  $2\lambda$  the spin splitting at the valence band top caused by the SOC,  $\hat{\sigma}$  are the Pauli matrices for the two basis functions, and  $\hat{s}_z$  is the Pauli matrix for spin<sup>1</sup>. The coupling strength of optical interband

---

<sup>1</sup>The spin-up and spin-down components are completely decoupled, meaning  $s_z$  remains a good quantum number.

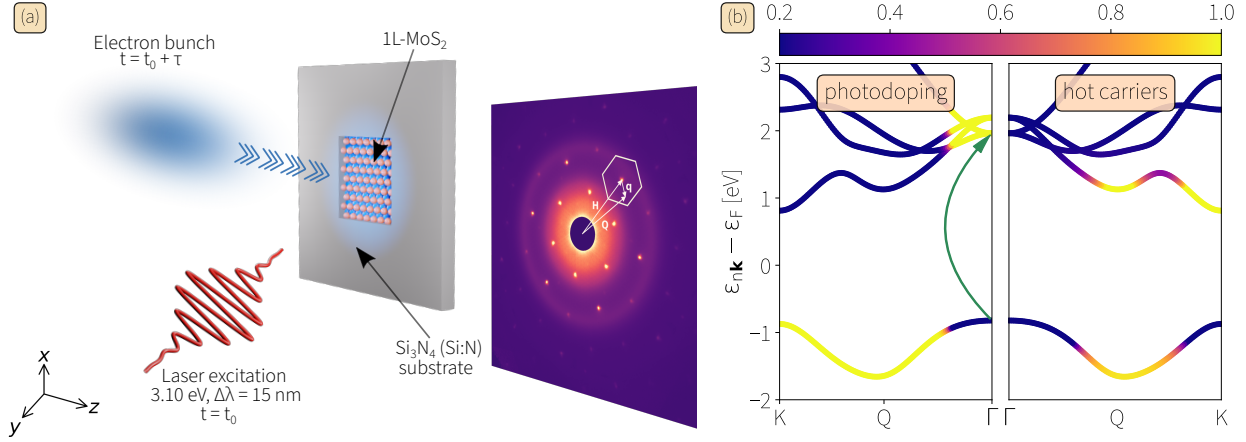


FIGURE 3.1: (a) Schematic of the pump-probe UED and UEDS experiment. The MoS<sub>2</sub> monolayer-Si<sub>3</sub>N<sub>4</sub> (Si:N) hereostructure is photoexcited (pumped) by an ultrashort laser pulse (400nm, 3.1 eV) at  $t = t_0$ . After a controllable delay time  $\tau$ , an ultrashort electron pulse probes the sample at normal incidence (in  $\hat{z}$ ), and transmission elastic/inelastic (phonon-diffuse) scattering is imaged at the detector (right). A representative Brillouin zone of 1L-MoS<sub>2</sub> with the Bragg peak H, the scattering vector Q, and reduced scattering vector q are indicated. (b) Schematic of the photodoped electron (hole) occupation (color bar) prepared via photoexcitation (left) and after rapid carrier-carrier thermalization (right). Hot carriers in the right panel are described by a Fermi-Dirac distribution at an elevated electronic temperature  $T_0^{\text{el}} \simeq 1700$ K.

transitions from the spin-split valence-band tops to the conduction band bottoms with the optical fields of  $\sigma_{\pm}$  circular polarization is given by  $\mathcal{P}_{\pm}(\mathbf{k}) = \mathcal{P}_x(\mathbf{k}) \pm i\mathcal{P}_y(\mathbf{k})$ , where:

$$\mathcal{P}_a(\mathbf{k}) \equiv m_0 \langle u_c(\mathbf{k}) | \frac{1}{\hbar} \frac{\partial \hat{H}}{\partial k_a} | u_v(\mathbf{k}) \rangle \quad (3.2)$$

is the interband matrix element of the canonical momentum operator and  $m_0$  is the free electron mass. For transitions near the  $K$  points, we find

$$|\mathcal{P}_{\pm}(\mathbf{k} \sim K)|^2 = \frac{m_0 a^2 t^2}{\hbar^2} \left( 1 \pm \zeta \frac{\Delta'}{\sqrt{\Delta'^2 + 4a^2 t^2 k^2}} \right)^2 \stackrel{\Delta' \gg \hbar k}{\approx} \frac{m_0^2 a^2 t^2}{\hbar^2} (1 \pm \zeta)^2 \quad (3.3)$$

with  $\Delta' \equiv \Delta - \zeta s_z \lambda$  being the spin-dependent band gap. Therefore, interband transitions are coupled exclusively with  $\sigma^{\pm}$  circularly polarized optical field at the  $K$  ( $K'$ ) valley [24]. In the intervalley scattering by phonons, the whole system has threefold rotational symmetry, implying the selection rule of the angular momentum quantum number  $\ell$ :

$$\ell_{c(v)}(K) - \ell_{c(v)}(K') = \pm 1 \quad (3.4)$$

by emitting a circular polarized valley phonon ( $\ell_{ph} = \pm 1$ ). Since the minimum of the conduction band valleys in 1L-MoS<sub>2</sub> are dominated by the  $\ell = 0$  d orbitals on the Mo atoms [28], they bear an overall azimuthal quantum number  $m_{\tau} = \tau = \pm 1$  at  $K$  ( $K'$ ). Likewise, the top of the valence bands have no azimuthal quantum number, so  $m = 0$ . Conservation of the pseudo-angular momentum (PAM) experienced by the system then dictates a selection rule  $\Delta m = \pm 1$ . By including the incidence of a photon, we can expand the selection rule to determine:

$$\Delta \ell_{\text{el}} = \pm \ell_{\text{ph}} \pm \ell_{\text{photon}} \quad (3.5)$$

where + is emission and - is absorption. This yields the following schema to generate chiral phonons.

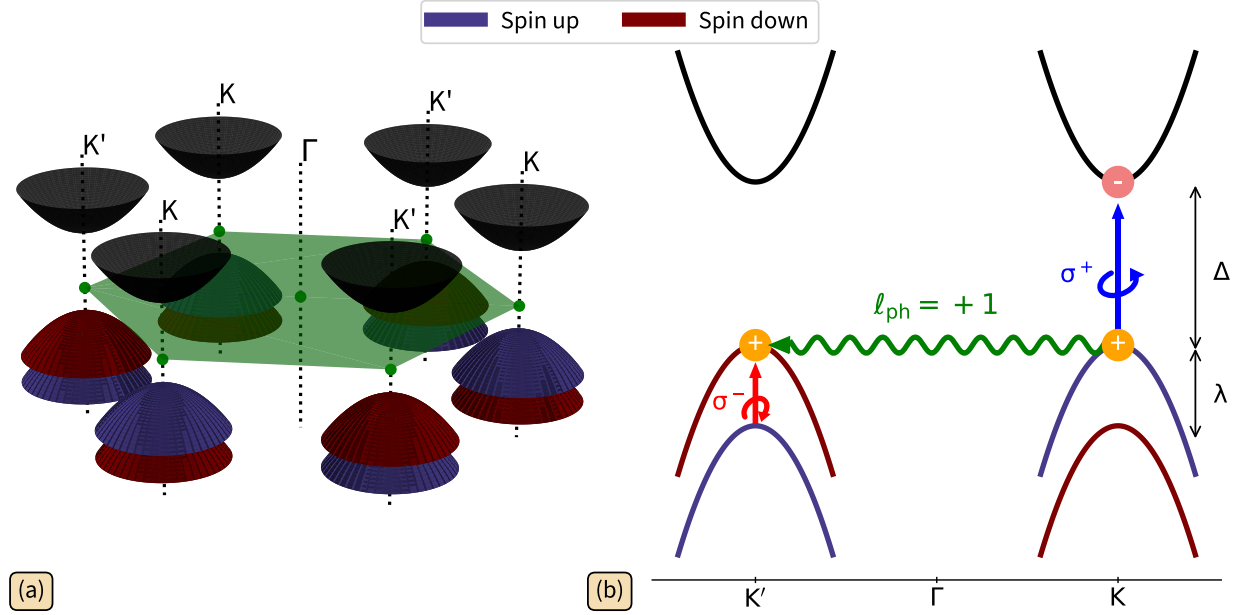


FIGURE 3.2: Excitation scheme for chiral phonons. (a) Approximate electronic band structure of a 2D honeycomb lattice near the valleys. The spin splitting is only appreciable in the valence band (on order of hundreds of meV). High symmetry points in the 2D BZ are labelled. (b) Exciton generation at  $K$  ( $K'$ ) occurs with  $\sigma^\pm$  excitation at energy  $\Delta$ , the bandgap. Subsequent stimulated absorption of a  $\sigma^\mp$  midIR photon will intervalley scatter the hole to the spin-conserving state via emission of a  $K$  ( $K'$ ) valley phonon of chirality  $\ell_{\text{ph}} = \pm 1$ . The hole is left in an excited state and is now only loosely coupled to its paired electron. In this configuration, intervalley biexcitons have been reported in these TMD systems [65].

- ▶  $\ell_{\text{ph}} = -1$

The exciton is excited by a right polarized photon with energy  $\Delta'$  at  $K$ . By absorbing a stimulated right-handed photon with energy  $\lambda + \hbar\omega$ , the excited hole in the valence band is scattered to the other valley  $K'$  by emitting a valley phonon with energy  $\hbar\omega$  and PAM  $\ell_{\text{ph}} = -1$ .

- ▶  $\ell_{\text{ph}} = +1$

The exciton is excited by a right polarized photon with energy  $\Delta'$  at  $K$ . A stimulated left-handed photon with energy  $\lambda + \hbar\omega$  is absorbed, and a valley phonon with energy  $\hbar\omega$  is emitted with PAM  $\ell_{\text{ph}} = +1$ .

Therefore, by optically exciting a sample with  $\sigma^\pm$  excitation, we can selectively generate chiral phonons of  $\ell_{\text{ph}} = \pm 1$  at the  $K$  ( $K'$ ) valleys, yielding a valley momentum anisotropy that is detectable in the UEDS signal (see Section 3.1.2.2). Up-conversion of our standard 800nm ultrafast laser pulse (see Figure 2.1) will be used to generate the exciton at  $K$  ( $K'$ ). A subsequent  $\sigma^\mp$  mid-infrared photon of energy  $\lambda + \hbar\omega$ , generated by the use of an optical parametric amplifier (OPA), will then induce scattering of the hole via the emission of a chiral phonon of pseudo-angular momentum  $\ell_{\text{ph}} = \pm 1$ , see Figure 3.2.

### 3.1.2.2 Observation of chiral phonons from UEDS

We plan to follow the following protocol to observe chiral phonons in 1L-MoS<sub>2</sub>. Firstly,  $\sigma^+$  excitation will create an exciton at  $K$ . Subsequent  $\sigma^\mp$  polarized midIR photoexcitation will then emit a chiral phonon of  $\ell_{\text{ph}} = \pm 1$ . In a generic 2D honeycomb lattice, there is only one phonon mode  $\nu$  that exhibits PAM of a given sign. For example,

in 1L-MoS<sub>2</sub>, only the LO<sub>1</sub> mode has chirality  $\pm 1$  at  $K$  ( $K'$ ), and inversely only the TO<sub>2</sub> mode has chirality  $\mp 1$  at  $K$  ( $K'$ ). By exploiting the momentum selection rule of the one-phonon structure factor in Eq. (2.3), we can isolate the dynamics of any given visible<sup>2</sup> mode based on their location in the diffraction pattern<sup>3</sup>. Therefore, we can exactly identify if either the LO<sub>1</sub> mode or TO<sub>2</sub> mode is preferentially occupied by midIR excitation of handedness  $\pm 1$ , and thus whether we observe emission of chiral phonons of PAM  $\pm 1$ . We can repeat the above observations by starting with exciton generation at the  $K'$  valley instead. The comparison to first-principles is yet to be planned completely, owing partially to the fact that the theory to do so has not entirely been developed. The difference in implementations compared to the linearly polarised 1L-MoS<sub>2</sub> experiments is that we will need to modify Eq. (2.7) to reflect the inhomogenous photodoping of carriers at  $K$  ( $K'$ ), as opposed to the current (easier) method of exciting charge carriers to the conduction manifold uniformly across the BZ.

### 3.1.3 Chapter 3: Thermoelectric SnSe

The second case we consider is bulk thermoelectric SnSe, a layered mono-chalcogen with much recent interest due to its extremely high thermoelectric figure of merit [66, 67], approaching that of the internal combustion engine. In a UEDS experiment on SnSe, we previously observed charge carrier relaxation in the valence and conduction manifold. Due to the strong anisotropic EPC of this polar material [68], we directly observed local, real-space distortion of the lattice associated with polaron formation following optical excitation (i.e. 'phonon-dressing' of the photo-generated carriers). This direct visualization of the lattice component of polaron formation is a first-of-its-kind measurement [57]. *Ab-initio* polaronic theory using density functional theory (DFT) methods has also only very recently been developed. I propose to use the *ab-initio* methodology of Sio *et al.* [69] to simulate polaron formation in SnSe and extract as before the computed change in diffraction intensity due to the polaron in a systematic study over the relevant range of temperatures ( $300\text{K} < T_c < 800\text{K}$ ). Being able to understand and even control the thermoelectric figure of merit of a material rivalling that of a car engine shows great industrial promise. Monolayer SnSe has even been suggested as a possible platform for ultrathin ferroelectrics comparable to similar behaviour in the pivotal solar cell material, lead halide perovskites [70].

The UEDS experiment on SnSe only requires examination of the diffuse intensity for phonon wavevectors  $\mathbf{q} \sim \Gamma$ , requiring less sensitivity than the momentum resolution required for the 1L experiments outlined previously, as polaron formation requires mainly low frequency acoustic displacements [57]. The comparison to *ab-initio* simulations will use the following approach.

The theory of Sio *et al.* [69] provides the atomic displacements necessary to form the electron or hole polaron, for all atoms  $\kappa$  at all unit cells  $c$  in terms of the phonon frequencies  $\omega_{\mathbf{q}\nu}$  and polarizations  $\{\mathbf{e}_{\mathbf{q}\nu}\}$  that can be simply added to the displacements created in the ZG special displacement method [71] of evaluating the LBJ dynamic diffuse structure factors in Eq. (2.8). Therefore, by propagating the TDBE, we can determine the occupations of all phonons, ergo their contribution to polaron formation at each time step  $\tau$ , thus determining the impact of dynamic polaron formation on the UEDS signal that we can observe experimentally.

## 3.2 TIMELINE

The proposed timeline is given in Figure 3.3. The primary experiment validating the extension of UEDS to monolayers and the first-principles methodology has already been performed and published (include citation for your mos2 paper). The next extension will be to recreate the experiment with selective circularly-polarised

<sup>2</sup>For example, with the electron beam at normal incidence, we cannot capture any dynamics resulting in phonons with atomic polarization vectors normal to the surface of the material / parallel to beam incidence.

<sup>3</sup>This approach was used to extract the individual dynamics of the LA, TA, LO, and TO modes of 1L-MoS<sub>2</sub>.

photoexcitation scheme outlined in [Figure 3.2](#). The experiments will hopefully be finished by the end of 2022, provided I am able to successfully operate the OPA.

After these experiments, the instrument will feature a sample mount that can control sample temperature from  $4\text{K} < T < 1000\text{K}$ , allowing for temperature-dependent UEDS experiments on SnSe around the phase transition (at temperature  $T_c$ ), where we aim to determine the impact of polaron formation on the drastic change in thermoelectric figure of merit around  $T_c$ . These experiments will not prove as difficult as the monolayer experiments, owing to the increase in SNR afforded by increased sample thickness. The challenge will be in implementing an *ab-initio* comparison to the experiments, which will be spearheaded by collaborators. At such time of these experiments, however, I aim to be knowledgeable enough to perform these simulations on my own. Nonetheless, our primary collaborators Fabio Caruso and Zacharias Giustino have agreed to collaborate for these calculations and lend their expertise to the development of this novel theory.

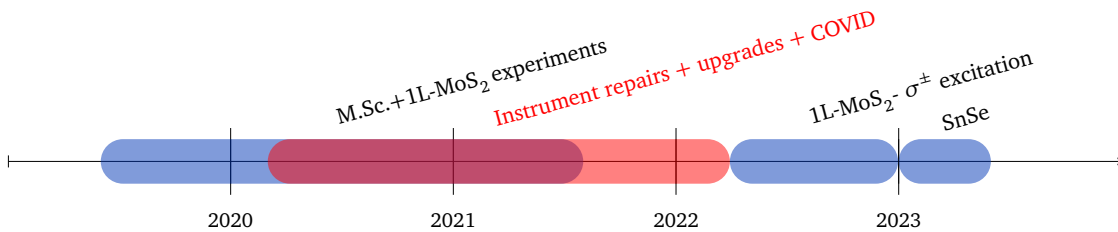


FIGURE 3.3: Timeline for the rest of the studies put forth in this proposal.

### 3.2.1 Additional experiments

Continuing to push the bounds of what UEDS is capable of observing, we are working with groups now to manufacture artificial heterostructures of various TMDs. Such samples include MoS<sub>2</sub>/WSe<sub>2</sub> bilayers, twist-angle heterostructures of these same materials, and the corresponding Moiré superlattices. No direct observation of EPC or the lattice dynamics in these combined systems have been reported to date using diffraction techniques, a gap we aim to fill throughout my PhD, time allowing.

# A

## *One phonon structure factor*

---

The one-phonon structure factor that forms part of the expression for phonon-diffuse intensity can be written:

$$|F_{1\nu}(\mathbf{Q}, \tau)|^2 = \left| \sum_{\kappa} e^{-W_{\kappa}(\mathbf{Q}, \tau)} \frac{f_{\kappa}(\mathbf{Q})}{\sqrt{\mu_{\kappa}}} (\mathbf{Q} \cdot \mathbf{e}_{q_{\nu\kappa}}) \right|^2 \quad (\text{A.1})$$

where  $\kappa$  indexes the atoms in the unit cell,  $W$  is the Debye-Waller factor,  $\mu_{\kappa}$  is the reduced mass of atom  $\kappa$ ,  $f_{\kappa}$  is the electron atomic form factor, and  $\mathbf{e}_{q_{\nu\kappa}}$  is the vector displacement of the  $\kappa^{\text{th}}$  atom in phonon mode  $\nu$  at momenta  $\mathbf{q}$ . The critical feature is the dot product, which shows the structure factors are optimal when the atomic polarizations are parallel to the scattering vector, and zero otherwise. It Furthermore is what allows for the identification of dynamics from individual phonon modes by examining specific regions of the diffuse intensity where structure factors for other modes may be zero.

# B

## Collision Integrals of the TDBE

---

We elucidate the theory of the collision integrals used in the propagation of the TDBE here. We write expressions for the electron-phonon collision integrals [58] as follows:

$$\begin{aligned} \Gamma_{n\mathbf{k}}^{\text{e-ph}}(f_{n\mathbf{k}}, n_{\mathbf{q}\nu}; \tau) &= \frac{2\pi}{\hbar} \sum_{mn} \int \frac{d\mathbf{q}}{\Omega_{\text{BZ}}} |g_{mn\nu}(\mathbf{k}, \mathbf{q})|^2 \\ &\times \left\{ (1 - f_{n\mathbf{k}}) f_{m\mathbf{k}+\mathbf{q}} \delta(\epsilon_{n\mathbf{k}} - \epsilon_{m\mathbf{k}+\mathbf{q}} + \hbar\omega_{\mathbf{q}\nu}) (1 + n_{\mathbf{q}\nu}) \right. \\ &+ (1 - f_{n\mathbf{k}}) f_{m\mathbf{k}+\mathbf{q}} \delta(\epsilon_{n\mathbf{k}} - \epsilon_{m\mathbf{k}+\mathbf{q}} - \hbar\omega_{\mathbf{q}\nu}) n_{\mathbf{q}\nu} \\ &- f_{n\mathbf{k}} (1 - f_{m\mathbf{k}+\mathbf{q}}) \delta(\epsilon_{n\mathbf{k}} - \epsilon_{m\mathbf{k}+\mathbf{q}} - \hbar\omega_{\mathbf{q}\nu}) (1 + n_{\mathbf{q}\nu}) \\ &\left. - f_{n\mathbf{k}} (1 - f_{m\mathbf{k}+\mathbf{q}}) \delta(\epsilon_{n\mathbf{k}} - \epsilon_{m\mathbf{k}+\mathbf{q}} + \hbar\omega_{\mathbf{q}\nu}) n_{\mathbf{q}\nu} \right\} \end{aligned} \quad (\text{B.1a})$$

$$\begin{aligned} \Gamma_{\mathbf{q}\nu}^{\text{ph-e}}(n_{\mathbf{q}\nu}, f_{n\mathbf{k}}; \tau) &= \frac{4\pi}{\hbar} \sum_{mn} \int \frac{d\mathbf{k}}{\Omega_{\text{BZ}}} |g_{mn\nu}(\mathbf{k}, \mathbf{q})|^2 \delta(\epsilon_{m\mathbf{k}+\mathbf{q}} - \epsilon_{n\mathbf{k}} - \hbar\omega_{\mathbf{q}\nu}) \\ &\times \left[ (1 - f_{n\mathbf{k}}) f_{m\mathbf{k}+\mathbf{q}} (n_{\mathbf{q}\nu} + 1) - f_{n\mathbf{k}} (1 - f_{m\mathbf{k}+\mathbf{q}}) n_{\mathbf{q}\nu} \right] \end{aligned} \quad (\text{B.1b})$$

It is important to note that Eqns B.1 directly depend on the amplitude of the EPC matrix elements, namely  $|g_{mn\nu}(\mathbf{k}, \mathbf{q})|^2$ , where  $m, n$  index the Kohn-Sham electronic eigenstates. Therefore any renormalization of the EPC strength will directly affect the propagation of the TBDE and the subsequent simulated diffraction intensity.

We compute the phonon-phonon collision integral  $\Gamma_{\mathbf{q}\nu}^{\text{ph-ph}}$  in the relaxation time approximation. In this manner, we can express this collision integral as:

$$\Gamma_{\mathbf{q}\nu}^{\text{ph-ph}}(n_{\mathbf{q}\nu}; \tau) \simeq \frac{n_{\mathbf{q}\nu}(\tau) - n_{\mathbf{q}\nu}^{\text{eq}}(\tau)}{\tau_{\mathbf{q}\nu}^{\text{ph-ph}}} \quad (\text{B.2})$$

where  $n^{\text{eq}}$  is the equilibrium distribution that arises at the effective temperature of the lattice at time  $\tau$ . Its time dependence arises from the constant exchange of energy between the vibrational and electronic systems, leading to changes in average temperature of the lattice. Furthermore,  $\tau_{\mathbf{q}\nu}^{\text{ph-ph}}$  is the phonon-phonon relaxation time at equilibrium, defined [72]:

$$\begin{aligned} \frac{1}{\tau_{\mathbf{q}\nu}^{\text{ph-ph}}} &\equiv \frac{\hbar\pi}{4} \sum_{\nu'\nu''} \int \frac{d\mathbf{q}'}{\Omega_{\text{BZ}}} \left| \Psi_{\mathbf{q}\mathbf{q}'\mathbf{q}''}^{\nu\nu'\nu''} \right|_+^2 (n_{\mathbf{q}'\nu'} - n_{\mathbf{q}''\nu''}) \delta(\omega_{\mathbf{q}\nu} + \omega_{\mathbf{q}'\nu'} - \omega_{\mathbf{q}''\nu''}) \delta_{\mathbf{q}+\mathbf{q}'-\mathbf{q}''}^G + \\ &\left| \Psi_{\mathbf{q}\mathbf{q}'\mathbf{q}''}^{\nu\nu'\nu''} \right|_-^2 (n_{\mathbf{q}'\nu'} + n_{\mathbf{q}''\nu''} + 1) \delta(\omega_{\mathbf{q}\nu} - \omega_{\mathbf{q}'\nu'} - \omega_{\mathbf{q}''\nu''}) \delta_{\mathbf{q}-\mathbf{q}'-\mathbf{q}''}^G \end{aligned} \quad (\text{B.3a})$$

$$\left| \Psi_{\mathbf{q}\mathbf{q}'\mathbf{q}''}^{\nu\nu'\nu''} \right|_{\pm}^2 = \sum_{i \in \text{u.c.}} \sum_{j,k} \sum_{\alpha\beta\gamma} \Phi_{ijk}^{\alpha\beta\gamma} \frac{(\mathbf{e}_{\mathbf{q}\nu i})^\alpha (\mathbf{e}_{\pm\mathbf{q}'\nu j})^\beta (\mathbf{e}_{-\mathbf{q}''\nu'' k})^\gamma}{\sqrt{M_i M_j M_k}} \quad (\text{B.3b})$$

$$\begin{aligned} \Phi_{ijk}^{\alpha\beta\gamma} &= \frac{\partial^3 H^{\text{KS}}}{\partial r_i^\alpha \partial r_j^\beta \partial r_k^\gamma} \simeq \frac{1}{2h} \left[ \frac{\partial^2 H^{\text{KS}}}{\partial r_j^\beta \partial r_k^\gamma} (r_i^\alpha = h) - \frac{\partial^2 H^{\text{KS}}}{\partial r_j^\beta \partial r_k^\gamma} (r_i^\alpha = -h) \right] \\ &\simeq \frac{1}{4h^2} \left[ -F_k^\gamma(r_i^\alpha = h, r_j^\beta = h) + F_k^\gamma(r_i^\alpha = h, r_j^\beta = -h) \right. \\ &\quad \left. + F_k^\gamma(r_i^\alpha = -h, r_j^\beta = h) - F_k^\gamma(r_i^\alpha = -h, r_j^\beta = -h) \right] \end{aligned} \quad (\text{B.3c})$$

where  $\left| \Psi_{\mathbf{q}\mathbf{q}'\mathbf{q}''}^{\nu\nu'\nu''} \right|_{\pm}^2$  is the 3-phonon scattering matrix elements of coalescing (emission) processes,  $i, j, k$  index the atomic types ( $i$  ranging only over the unit cell),  $\alpha, \beta, \gamma$  are Cartesian indices,  $M$  the atomic mass,  $(\mathbf{e}_{\mathbf{q}\nu i})^\alpha$  the  $\alpha^{\text{th}}$  component of the atomic eigendisplacement of the  $i^{\text{th}}$  atom at momentum  $\mathbf{q}$  in mode  $\nu$ , and  $\Phi$  the third-order interatomic force constant.  $H^{\text{KS}}$  the Kohn-Sham DFT Hamiltonian of the perturbed system, and  $r_i^\alpha$  the  $\alpha^{\text{th}}$  component of the displacement from equilibrium of the  $i^{\text{th}}$  atom<sup>1</sup>, with  $F_k^\gamma$  the  $\gamma$  component of the force felt on atom  $k$  under component-wise displacements of atoms  $i$  and  $j$  by  $\pm h$ , with  $h \ll 1$ .

At thermal equilibrium ( $T_0^{\text{el}} = T_0^{\text{ph}}$ ), the system is stable, and each population will remain constant. However, as  $T_0^{\text{el}} > T_0^{\text{ph}}$ , electron-phonon interactions will start to drive the system back to equilibrium. Such a condition is created in the UEDS experiment, and so both approaches are suited to probe the dynamics of EPC-induced effects.

---

<sup>1</sup>These force constants are determined by resolving an irreducible set of atomic displacements from which to compute the full anharmonic matrix.

# Bibliography

---

- [1] K. S. Novoselov, A. K. Geim, S. V. Morozov, D. Jiang, Y. Zhang, S. V. Dubonos, I. V. Grigorieva, and A. A. Firsov. “Electric Field Effect in Atomically Thin Carbon Films”. In: *Science* 306.5696 (2004), pp. 666–669. DOI: [10.1126/science.1102896](https://doi.org/10.1126/science.1102896). eprint: <https://www.science.org/doi/pdf/10.1126/science.1102896>. URL: <https://www.science.org/doi/abs/10.1126/science.1102896> (cit. on p. 1).
- [2] Nicolas Mounet, Marco Gibertini, Philippe Schwaller, Davide Campi, Andrius Merkys, Antimo Marrazzo, Thibault Sohier, Ivano Eligio Castelli, Andrea Cepellotti, Giovanni Pizzi, and Nicola Marzari. “Two-dimensional materials from high-throughput computational exfoliation of experimentally known compounds”. In: *Nature Nanotechnology* 13.3 (2018), pp. 246–252. ISSN: 1748-3395. DOI: [10.1038/s41565-017-0035-5](https://doi.org/10.1038/s41565-017-0035-5). URL: <https://doi.org/10.1038/s41565-017-0035-5> (cit. on p. 1).
- [3] R. Rossetti, S. Nakahara, and L. E. Brus. “Quantum size effects in the redox potentials, resonance Raman spectra, and electronic spectra of CdS crystallites in aqueous solution”. In: *The Journal of Chemical Physics* 79.2 (1983), pp. 1086–1088. DOI: [10.1063/1.445834](https://doi.org/10.1063/1.445834). eprint: <https://doi.org/10.1063/1.445834>. URL: <https://doi.org/10.1063/1.445834> (cit. on p. 1).
- [4] J.O. Island and A. Castellanos-Gomez. “Chapter Seven - Black Phosphorus-Based Nanodevices”. In: *2D Materials*. Ed. by Francesca Iacopi, John J. Boeckl, and Chennupati Jagadish. Vol. 95. Semiconductors and Semimetals. Elsevier, 2016, pp. 279–303. DOI: <https://doi.org/10.1016/bs.semsem.2016.03.002>. URL: <https://www.sciencedirect.com/science/article/pii/S0080878416300023> (cit. on p. 1).
- [5] F. Reis, G. Li, L. Dudy, M. Bauernfeind, S. Glass, W. Hanke, R. Thomale, J. Schäfer, and R. Claessen. “Bismuthene on a SiC substrate: A candidate for a high-temperature quantum spin Hall material”. In: *Science* 357.6348 (2017), pp. 287–290. DOI: [10.1126/science.aai8142](https://doi.org/10.1126/science.aai8142). eprint: <https://www.science.org/doi/pdf/10.1126/science.aai8142>. URL: <https://www.science.org/doi/abs/10.1126/science.aai8142> (cit. on p. 1).
- [6] Xu Wu, Yan Shao, Hang Liu, Zili Feng, Ye-Liang Wang, Jia-Tao Sun, Chen Liu, Jia-Ou Wang, Zhong-Liu Liu, Shi-Yu Zhu, Yu-Qi Wang, Shi-Xuan Du, You-Guo Shi, Kurash Ibrahim, and Hong-Jun Gao. “Epitaxial Growth and Air-Stability of Monolayer Antimonene on PdTe<sub>2</sub>”. In: *Advanced Materials* 29.11 (2017), p. 1605407. DOI: <https://doi.org/10.1002/adma.201605407>. eprint: <https://onlinelibrary.wiley.com/doi/pdf/10.1002/adma.201605407>. URL: <https://onlinelibrary.wiley.com/doi/abs/10.1002/adma.201605407> (cit. on p. 1).
- [7] Changgu Lee, Xiaoding Wei, Jeffrey W. Kysar, and James Hone. “Measurement of the Elastic Properties and Intrinsic Strength of Monolayer Graphene”. In: *Science* 321.5887 (2008), pp. 385–388. DOI: [10.1126/science.1157996](https://doi.org/10.1126/science.1157996). eprint: <https://www.science.org/doi/pdf/10.1126/science.1157996>. URL: <https://www.science.org/doi/abs/10.1126/science.1157996> (cit. on p. 2).
- [8] Archana Raja, Andrey Chaves, Jae-eun Yu, Ghidewon Arefe, Heather M. Hill, Albert F. Rigosi, Timothy C. Berkelbach, Philipp Nagler, Christian Schüller, Tobias Korn, Colin Nuckolls, James Hone, Louis E. Brus, Tony F. Heinz, David R. Reichman, and Alexey Chernikov. “Coulomb engineering of the bandgap and excitons in two-dimensional materials”. In: *Nature Communications* 8.1 (2017), p. 15251. ISSN: 2041-1723. DOI: [10.1038/ncomms15251](https://doi.org/10.1038/ncomms15251). URL: <https://doi.org/10.1038/ncomms15251> (cit. on p. 2).
- [9] Fang Liu, Mark E. Ziffer, Kameron R. Hansen, Jue Wang, and Xiaoyang Zhu. “Direct Determination of Band-Gap Renormalization in the Photoexcited Monolayer MoS<sub>2</sub>”. In: *Phys. Rev. Lett.* 122 (24 2019), p. 246803. DOI: [10.1103/PhysRevLett.122.246803](https://doi.org/10.1103/PhysRevLett.122.246803). URL: <https://link.aps.org/doi/10.1103/PhysRevLett.122.246803> (cit. on pp. 2, 3).
- [10] Yang Song and Hanan Dery. “Transport Theory of Monolayer Transition-Metal Dichalcogenides through Symmetry”. In: *Phys. Rev. Lett.* 111 (2 2013), p. 026601. DOI: [10.1103/PhysRevLett.111.026601](https://doi.org/10.1103/PhysRevLett.111.026601). URL: <https://link.aps.org/doi/10.1103/PhysRevLett.111.026601> (cit. on pp. 2, 3).
- [11] Nan Zhang, Alessandro Surrente, Michał Baranowski, Duncan K Maude, Patricia Gant, Andres Castellanos-Gomez, and Paulina Plochocka. “Moiré intralayer excitons in a MoSe<sub>2</sub>/MoS<sub>2</sub> heterostructure”. In: *Nano letters* 18.12 (2018), pp. 7651–7657. DOI: <https://doi.org/10.1021/acs.nanolett.8b03266>. URL: <https://pubs.acs.org/doi/10.1021/acs.nanolett.8b03266> (cit. on pp. 2, 3).
- [12] Marco Bernardi, Maurizia Palummo, and Jeffrey C. Grossman. “Extraordinary Sunlight Absorption and One Nanometer Thick Photovoltaics Using Two-Dimensional Monolayer Materials”. In: *Nano Letters* 13.8 (2013). PMID: 23750910, pp. 3664–3670. DOI: [10.1021/nl401544y](https://doi.org/10.1021/nl401544y). eprint: <https://doi.org/10.1021/nl401544y>. URL: <https://doi.org/10.1021/nl401544y> (cit. on p. 2).
- [13] Oriol Lopez-Sanchez, Dominik Lembke, Metin Kayci, Aleksandra Radenovic, and Andras Kis. “Ultrasensitive photodetectors based on monolayer MoS<sub>2</sub>”. In: *Nature Nanotechnology* 8.7 (2013), pp. 497–501. ISSN: 1748-3395. DOI: [10.1038/nnano.2013.100](https://doi.org/10.1038/nnano.2013.100). URL: <https://doi.org/10.1038/nnano.2013.100> (cit. on p. 2).

- [14] Wenjing Zhang, Chih-Piao Chuu, Jing-Kai Huang, Chang-Hsiao Chen, Meng-Lin Tsai, Yung-Huang Chang, Chi-Te Liang, Yu-Ze Chen, Yu-Lun Chueh, Jr-Hau He, Mei-Yin Chou, and Lain-Jong Li. "Ultrahigh-Gain Photodetectors Based on Atomically Thin Graphene-MoS<sub>2</sub> Heterostructures". In: *Scientific Reports* 4.1 (2014), p. 3826. ISSN: 2045-2322. DOI: [10.1038/srep03826](https://doi.org/10.1038/srep03826). URL: <https://doi.org/10.1038/srep03826> (cit. on p. 2).
- [15] Sonali Das, Deepak Pandey, Jayan Thomas, and Tania Roy. "The Role of Graphene and Other 2D Materials in Solar Photovoltaics". In: *Advanced Materials* 31.1 (2019), p. 1802722. DOI: <https://doi.org/10.1002/adma.201802722>. eprint: <https://onlinelibrary.wiley.com/doi/pdf/10.1002/adma.201802722>. URL: <https://onlinelibrary.wiley.com/doi/abs/10.1002/adma.201802722> (cit. on p. 3).
- [16] Stephen J. Fonash. "Chapter Two - Material Properties and Device Physics Basic to Photovoltaics". In: *Solar Cell Device Physics (Second Edition)*. Ed. by Stephen J. Fonash. Second Edition. Boston: Academic Press, 2010, pp. 9–65. ISBN: 978-0-12-374774-7. DOI: <https://doi.org/10.1016/B978-0-12-374774-7.00002-9>. URL: <https://www.sciencedirect.com/science/article/pii/B9780123747747000029> (cit. on p. 3).
- [17] Yuan Cao, Valla Fatemi, Shiang Fang, Kenji Watanabe, Takashi Taniguchi, Efthimios Kaxiras, and Pablo Jarillo-Herrero. "Unconventional superconductivity in magic-angle graphene superlattices". In: *Nature* 556.7699 (2018), pp. 43–50. ISSN: 1476-4687. DOI: [10.1038/nature26160](https://doi.org/10.1038/nature26160). URL: <https://doi.org/10.1038/nature26160> (cit. on p. 3).
- [18] Jiamin Quan, Lukas Linhart, Miao-Ling Lin, Daehun Lee, Jihang Zhu, Chun-Yuan Wang, Wei-Ting Hsu, Junho Choi, Jacob Embley, Carter Young, et al. "Phonon renormalization in reconstructed MoS<sub>2</sub> moiré superlattices". In: *Nature materials* (2021), pp. 1–6. DOI: <https://doi.org/10.1038/s41563-021-00960-1>. URL: <https://www.nature.com/articles/s41563-021-00960-1> (cit. on p. 3).
- [19] Simone Latini, Kirsten T. Winther, Thomas Olsen, and Kristian S. Thygesen. "Interlayer Excitons and Band Alignment in MoS<sub>2</sub>/hBN/WSe<sub>2</sub> van der Waals Heterostructures". In: *Nano Letters* 17.2 (2017). PMID: 28026961, pp. 938–945. DOI: [10.1021/acs.nanolett.6b04275](https://doi.org/10.1021/acs.nanolett.6b04275). eprint: <https://doi.org/10.1021/acs.nanolett.6b04275>. URL: <https://doi.org/10.1021/acs.nanolett.6b04275> (cit. on p. 3).
- [20] Ioannis Paradisanos, Shivangi Shree, Antony George, Nadine Leisgang, Cedric Robert, Kenji Watanabe, Takashi Taniguchi, Richard J. Warburton, Andrey Turchanin, Xavier Marie, Iann C. Gerber, and Bernhard Urbaszek. "Controlling interlayer excitons in MoS<sub>2</sub> layers grown by chemical vapor deposition". In: *Nature Communications* 11.1 (2020), p. 2391. ISSN: 2041-1723. DOI: [10.1038/s41467-020-16023-z](https://doi.org/10.1038/s41467-020-16023-z). URL: <https://doi.org/10.1038/s41467-020-16023-z> (cit. on p. 3).
- [21] Di Huang, Junho Choi, Chih-Kang Shih, and Xiaoqin Li. "Excitons in semiconductor moiré superlattices". In: *Nature Nanotechnology* 17.3 (2022), pp. 227–238. ISSN: 1748-3395. DOI: [10.1038/s41565-021-01068-y](https://doi.org/10.1038/s41565-021-01068-y). URL: <https://doi.org/10.1038/s41565-021-01068-y> (cit. on p. 3).
- [22] Benjamin T. Zhou, Katsuhisa Taguchi, Yuki Kawaguchi, Yukio Tanaka, and K. T. Law. "Spin-orbit coupling induced valley Hall effects in transition-metal dichalcogenides". In: *Communications Physics* 2.1 (2019), p. 26. ISSN: 2399-3650. DOI: [10.1038/s42005-019-0127-7](https://doi.org/10.1038/s42005-019-0127-7). URL: <https://doi.org/10.1038/s42005-019-0127-7> (cit. on p. 3).
- [23] Alejandro Molina-Sánchez, Davide Sangalli, Kerstin Hummer, Andrea Marini, and Ludger Wirtz. "Effect of spin-orbit interaction on the optical spectra of single-layer, double-layer, and bulk MoS<sub>2</sub>". In: *Phys. Rev. B* 88 (4 2013), p. 045412. DOI: [10.1103/PhysRevB.88.045412](https://doi.org/10.1103/PhysRevB.88.045412). URL: <https://link.aps.org/doi/10.1103/PhysRevB.88.045412> (cit. on p. 3).
- [24] Di Xiao, Gui-Bin Liu, Wanxiang Feng, Xiaodong Xu, and Wang Yao. "Coupled Spin and Valley Physics in Monolayers of MoS<sub>2</sub> and Other Group-VI Dichalcogenides". In: *Phys. Rev. Lett.* 108 (19 2012), p. 196802. DOI: [10.1103/PhysRevLett.108.196802](https://doi.org/10.1103/PhysRevLett.108.196802). URL: <https://link.aps.org/doi/10.1103/PhysRevLett.108.196802> (cit. on pp. 3, 11).
- [25] H. Beyer, G. Rohdeabo, familyi=v, giveni=A., giveni=A., „A. Stange, T. Jacobsen, L. Bignardi, D. Lizzit, P. Lacovig, C. E. Sanders, S. Lizzit, K. Rossnagel, P. Hofmann, and M. Bauer. "80% Valley Polarization of Free Carriers in Singly Oriented Single-Layer WS<sub>2</sub> on Au(111)". In: *Phys. Rev. Lett.* 123 (23 2019), p. 236802. DOI: [10.1103/PhysRevLett.123.236802](https://doi.org/10.1103/PhysRevLett.123.236802). URL: <https://link.aps.org/doi/10.1103/PhysRevLett.123.236802> (cit. on p. 3).
- [26] Diana Y. Qiu, Felipe H. da Jornada, and Steven G. Louie. "Optical Spectrum of MoS<sub>2</sub>: Many-Body Effects and Diversity of Exciton States". In: *Phys. Rev. Lett.* 111 (21 2013), p. 216805. DOI: [10.1103/PhysRevLett.111.216805](https://doi.org/10.1103/PhysRevLett.111.216805). URL: <https://link.aps.org/doi/10.1103/PhysRevLett.111.216805> (cit. on p. 3).
- [27] Wang Yao, Di Xiao, and Qian Niu. "Valley-dependent optoelectronics from inversion symmetry breaking". In: *Phys. Rev. B* 77 (23 2008), p. 235406. DOI: [10.1103/PhysRevB.77.235406](https://doi.org/10.1103/PhysRevB.77.235406). URL: <https://link.aps.org/doi/10.1103/PhysRevB.77.235406> (cit. on p. 3).

- [28] Eugene S. Kadantsev and Paweł Hawrylak. “Electronic structure of a single MoS<sub>2</sub> monolayer”. In: *Solid State Communications* 152.10 (2012), pp. 909–913. ISSN: 0038-1098. DOI: <https://doi.org/10.1016/j.ssc.2012.02.005>. URL: <https://www.sciencedirect.com/science/article/pii/S0038109812000889> (cit. on pp. 3, 11).
- [29] Lifa Zhang and Qian Niu. “Chiral phonons at high-symmetry points in monolayer hexagonal lattices”. In: *Physical review letters* 115.11 (2015), p. 115502. DOI: <http://dx.doi.org/10.1103/PhysRevLett.115.115502>. URL: <https://journals.aps.org/prl/abstract/10.1103/PhysRevLett.115.115502> (cit. on p. 3).
- [30] Hanyu Zhu, Jun Yi, Ming-Yang Li, Jun Xiao, Lifa Zhang, Chih-Wen Yang, Robert A Kaindl, Lain-Jong Li, Yuan Wang, and Xiang Zhang. “Observation of chiral phonons”. In: *Science* 359.6375 (2018), pp. 579–582. DOI: <DOI:10.1126/science.aar2711>. URL: <https://www.science.org/doi/10.1126/science.aar2711> (cit. on p. 3).
- [31] Halleh B Balch, Austin M Evans, Raghunath R Dasari, Hong Li, Ruofan Li, Simil Thomas, Danqing Wang, Ryan P Bisbey, Kaitlin Slicker, Ioannina Castano, et al. “Electronically Coupled 2D Polymer/MoS<sub>2</sub> Heterostructures”. In: *Journal of the American Chemical Society* 142.50 (2020), pp. 21131–21139. DOI: <https://doi.org/10.1021/jacs.0c10151>. URL: <https://pubs.acs.org/doi/10.1021/jacs.0c10151> (cit. on p. 3).
- [32] Indrajit Maity, Arash A Mostofi, and Johannes Lischner. “Chiral valley phonons and flat phonon bands in moire materials”. In: *Physical Review B* 105.4 (2022), p. L041408. DOI: <https://doi.org/10.1103/PhysRevB.105.L041408>. URL: <https://journals.aps.org/prb/abstract/10.1103/PhysRevB.105.L041408> (cit. on p. 3).
- [33] Daniel J Trainer, BaoKai Wang, Fabrizio Bobba, Noah Samuelson, Xiaoxing Xi, John Zasadzinski, Jouko Nieminen, Arun Bansil, and Maria Iavarone. “Proximity-induced superconductivity in monolayer MoS<sub>2</sub>”. In: *ACS nano* 14.3 (2020), pp. 2718–2728. DOI: <https://doi.org/10.1021/acsnano.9b07475>. URL: <https://pubs.acs.org/doi/10.1021/acsnano.9b07475> (cit. on p. 3).
- [34] Sven Borghardt, Jhih-Sian Tu, Florian Winkler, Jürgen Schubert, Willi Zander, Kristjan Leosson, and Beata E Karolina Kardynał. “Engineering of optical and electronic band gaps in transition metal dichalcogenide monolayers through external dielectric screening”. In: *Physical review materials* 1.5 (2017), p. 054001. DOI: <https://doi.org/10.1103/PhysRevMaterials.1.054001>. URL: <https://journals.aps.org/prmaterials/abstract/10.1103/PhysRevMaterials.1.054001> (cit. on p. 3).
- [35] Feliciano Giustino. “Electron-phonon interactions from first principles”. In: *Rev. Mod. Phys.* 89 (1 2017), p. 015003. DOI: <10.1103/RevModPhys.89.015003>. URL: <https://link.aps.org/doi/10.1103/RevModPhys.89.015003> (cit. on p. 3).
- [36] A. Sauer, D. A. Zocco, A. H. Said, R. Heid, A. Böhmer, and F. Weber. “Electron-phonon coupling and superconductivity-induced distortion of the phonon lineshape in V<sub>3</sub>Si”. In: *Phys. Rev. B* 99 (13 2019), p. 134511. DOI: <10.1103/PhysRevB.99.134511>. URL: <https://link.aps.org/doi/10.1103/PhysRevB.99.134511> (cit. on p. 3).
- [37] Martin R. Otto, Jan-Hendrik Pöhls, Laurent P René de Cotret, Mark J. Stern, Mark Sutton, and Bradley J. Siwick. “Mechanisms of electron-phonon coupling unraveled in momentum and time: The case of soft phonons in TiSe<sub>2</sub>”. In: *Science Advances* 7.20 (2021). DOI: <10.1126/sciadv.abf2810>. URL: <https://advances.sciencemag.org/content/7/20/eabf2810> (cit. on pp. 3, 7).
- [38] Jin-Jian Zhou, Olle Hellman, and Marco Bernardi. “Electron-Phonon Scattering in the Presence of Soft Modes and Electron Mobility in SrTiO<sub>3</sub> Perovskite from First Principles”. In: *Phys. Rev. Lett.* 121 (22 2018), p. 226603. DOI: <10.1103/PhysRevLett.121.226603>. URL: <https://link.aps.org/doi/10.1103/PhysRevLett.121.226603> (cit. on p. 3).
- [39] Xiaoyang Zhu, Nicholas R. Monahan, Zizhou Gong, Haiming Zhu, Kristopher W. Williams, and Cory A. Nelson. “Charge Transfer Excitons at van der Waals Interfaces”. In: *Journal of the American Chemical Society* 137.26 (2015). PMID: 26001297, pp. 8313–8320. DOI: <10.1021/jacs.5b03141>. eprint: <https://doi.org/10.1021/jacs.5b03141>. URL: <https://doi.org/10.1021/jacs.5b03141> (cit. on p. 3).
- [40] Minhao He, Pasqual Rivera, Dinh Van Tuan, et al. “Valley phonons and exciton complexes in a monolayer semiconductor”. In: *Nature Communications* 11.1 (2020), p. 618. ISSN: 2041-1723. DOI: <10.1038/s41467-020-14472-0>. URL: <https://doi.org/10.1038/s41467-020-14472-0> (cit. on p. 3).
- [41] Fang Liu, Wenjing Wu, Yusong Bai, Sang Hoon Chae, Qiuyang Li, Jue Wang, James Hone, and X.-Y. Zhu. “Disassembling 2D van der Waals crystals into macroscopic monolayers and reassembling into artificial lattices”. In: *Science* 367.6480 (2020), pp. 903–906. DOI: <10.1126/science.aba1416>. eprint: <https://www.science.org/doi/pdf/10.1126/science.aba1416>. URL: <https://www.science.org/doi/abs/10.1126/science.aba1416> (cit. on p. 4).
- [42] Christopher A. Howard. “Exfoliating large monolayers in liquids”. In: *Nature Materials* 20.2 (2021), pp. 130–131. ISSN: 1476-4660. DOI: <10.1038/s41563-020-00907-y>. URL: <https://doi.org/10.1038/s41563-020-00907-y> (cit. on p. 4).

- [43] Yung-Huang Chang, Wenjing Zhang, Yihan Zhu, Yu Han, Jiang Pu, Jan-Kai Chang, Wei-Ting Hsu, Jing-Kai Huang, Chang-Lung Hsu, Ming-Hui Chiu, Taishi Takenobu, Henan Li, Chih-I Wu, Wen-Hao Chang, Andrew Thye Shen Wee, and Lain-Jong Li. "Monolayer MoSe<sub>2</sub> Grown by Chemical Vapor Deposition for Fast Photodetection". In: *ACS Nano* 8.8 (2014). PMID: 25094022, pp. 8582–8590. DOI: [10.1021/nn503287m](https://doi.org/10.1021/nn503287m). eprint: <https://doi.org/10.1021/nn503287m>. URL: <https://doi.org/10.1021/nn503287m> (cit. on p. 4).
- [44] Johannes Kepler. *Strene Seu de Nive Sexangula*. Francofurti ad Moenvm : Apud Godefridum Tampach, 1611 (cit. on p. 5).
- [45] W. Friedrich, P. Knipping, and M. Laue. "Interferenzerscheinungen bei Röntgenstrahlen". In: *Annalen der Physik* 346.10 (1913), pp. 971–988. DOI: <https://doi.org/10.1002/andp.19133461004>. eprint: <https://onlinelibrary.wiley.com/doi/pdf/10.1002/andp.19133461004>. URL: <https://onlinelibrary.wiley.com/doi/abs/10.1002/andp.19133461004> (cit. on p. 5).
- [46] G. P. THOMSON and A. REID. "Diffraction of Cathode Rays by a Thin Film". In: *Nature* 119.3007 (1927), pp. 890–890. ISSN: 1476-4687. DOI: [10.1038/119890a0](https://doi.org/10.1038/119890a0). URL: <https://doi.org/10.1038/119890a0> (cit. on p. 5).
- [47] C. J. Davisson and L. H. Germer. "Reflection of Electrons by a Crystal of Nickel". In: *Proceedings of the National Academy of Sciences* 14.4 (1928), pp. 317–322. DOI: [10.1073/pnas.14.4.317](https://doi.org/10.1073/pnas.14.4.317). eprint: <https://www.pnas.org/doi/pdf/10.1073/pnas.14.4.317>. URL: <https://www.pnas.org/doi/abs/10.1073/pnas.14.4.317> (cit. on p. 5).
- [48] "Scattering". In: *Transmission Electron Microscopy and Diffractometry of Materials*. Berlin, Heidelberg: Springer Berlin Heidelberg, 2008, pp. 119–162. ISBN: 978-3-540-73886-2. DOI: [10.1007/978-3-540-73886-2\\_3](https://doi.org/10.1007/978-3-540-73886-2_3). URL: [https://doi.org/10.1007/978-3-540-73886-2\\_3](https://doi.org/10.1007/978-3-540-73886-2_3) (cit. on p. 5).
- [49] Lutz Waldecker, Roman Bertoni, Ralph Ernstorfer, and Jan Vorberger. "Electron-Phonon Coupling and Energy Flow in a Simple Metal beyond the Two-Temperature Approximation". In: *Phys. Rev. X* 6 (2 2016), p. 021003. DOI: [10.1103/PhysRevX.6.021003](https://doi.org/10.1103/PhysRevX.6.021003). URL: <https://link.aps.org/doi/10.1103/PhysRevX.6.021003> (cit. on p. 6).
- [50] Marios Zacharias, Hélène Seiler, Fabio Caruso, Daniela Zahn, Feliciano Giustino, Pantelis C Kelires, and Ralph Ernstorfer. "Efficient first-principles methodology for the calculation of the all-phonon inelastic scattering in solids". In: *Physical review letters* 127.20 (2021), p. 207401 (cit. on pp. 6–8).
- [51] Marios Zacharias, Hélène Seiler, Fabio Caruso, Daniela Zahn, Feliciano Giustino, Pantelis C. Kelires, and Ralph Ernstorfer. "Multiphonon diffuse scattering in solids from first principles: Application to layered crystals and two-dimensional materials". In: *Phys. Rev. B* 104 (20 2021), p. 205109. DOI: [10.1103/PhysRevB.104.205109](https://doi.org/10.1103/PhysRevB.104.205109). URL: <https://link.aps.org/doi/10.1103/PhysRevB.104.205109> (cit. on pp. 6–9).
- [52] M. R. Otto, L. P. René de Cotret, M. J. Stern, and B. J. Siwick. "Solving the jitter problem in microwave compressed ultrafast electron diffraction instruments: Robust sub-50 fs cavity-laser phase stabilization". In: *Structural Dynamics* 4.5 (2017), p. 051101. DOI: [10.1063/1.4989960](https://doi.org/10.1063/1.4989960). eprint: <https://doi.org/10.1063/1.4989960>. URL: <https://doi.org/10.1063/1.4989960> (cit. on p. 6).
- [53] Mark J. Stern, Laurent P. René de Cotret, Martin R. Otto, Robert P. Chatelain, Jean-Philippe Boisvert, Mark Sutton, and Bradley J. Siwick. "Mapping momentum-dependent electron-phonon coupling and nonequilibrium phonon dynamics with ultrafast electron diffuse scattering". In: *Phys. Rev. B* 97 (16 2018), p. 165416. DOI: [10.1103/PhysRevB.97.165416](https://doi.org/10.1103/PhysRevB.97.165416). URL: <https://link.aps.org/doi/10.1103/PhysRevB.97.165416> (cit. on p. 7).
- [54] L. Waldecker, R. Bertoni, H. Hübener, T. Brumme, T. Vasileiadis, D. Zahn, A. Rubio, and R. Ernstorfer. "Momentum-Resolved View of Electron-Phonon Coupling in Multilayer WSe<sub>2</sub>". In: *Phys. Rev. Lett.* 119 (3 2017), p. 036803. DOI: [10.1103/PhysRevLett.119.036803](https://doi.org/10.1103/PhysRevLett.119.036803). URL: <https://link.aps.org/doi/10.1103/PhysRevLett.119.036803> (cit. on p. 7).
- [55] Hermann A. Dürr, Ralph Ernstorfer, and Bradley J. Siwick. "Revealing momentum-dependent electron-phonon and phonon-phonon coupling in complex materials with ultrafast electron diffuse scattering". In: *MRS Bulletin* 46.8 (2021), pp. 731–737. ISSN: 1938-1425. DOI: [10.1557/s43577-021-00156-7](https://doi.org/10.1557/s43577-021-00156-7). URL: <https://doi.org/10.1557/s43577-021-00156-7> (cit. on p. 7).
- [56] Hélène Seiler, Daniela Zahn, Marios Zacharias, Patrick-Nigel Hildebrandt, Thomas Vasileiadis, Yoav William Windsor, Yingpeng Qi, Christian Carbogno, Claudia Draxl, Ralph Ernstorfer, and Fabio Caruso. "Accessing the Anisotropic Nonthermal Phonon Populations in Black Phosphorus". In: *Nano Letters* 21.14 (2021). PMID: 34279103, pp. 6171–6178. DOI: [10.1021/acs.nanolett.1c01786](https://doi.org/10.1021/acs.nanolett.1c01786). eprint: <https://doi.org/10.1021/acs.nanolett.1c01786>. URL: <https://doi.org/10.1021/acs.nanolett.1c01786> (cit. on p. 7).

- [57] Laurent P René de Cotret, Martin R. Otto, Jan-Hendrik Pöhls, Zhongzhen Luo, Mercouri G. Kanatzidis, and Bradley J. Siwick. “Direct visualization of polaron formation in the thermoelectric SnSe”. In: *Proceedings of the National Academy of Sciences* 119.3 (2022), e2113967119. doi: [10.1073/pnas.2113967119](https://doi.org/10.1073/pnas.2113967119). eprint: <https://www.pnas.org/doi/pdf/10.1073/pnas.2113967119>. URL: <https://www.pnas.org/doi/abs/10.1073/pnas.2113967119> (cit. on pp. 7, 13).
- [58] Fabio Caruso. “Nonequilibrium Lattice Dynamics in Monolayer MoS<sub>2</sub>”. In: *The Journal of Physical Chemistry Letters* 12.6 (2021). PMID: 33569950, pp. 1734–1740. doi: [10.1021/acs.jpclett.0c03616](https://doi.org/10.1021/acs.jpclett.0c03616). URL: <https://doi.org/10.1021/acs.jpclett.0c03616> (cit. on pp. 7, 8, 16).
- [59] Jean Laval. “Étude expérimentale de la diffusion des rayons X par les cristaux”. In: *Bulletin de Minéralogie* 62.4 (1939), pp. 137–253. doi: [10.3406/bulmi.1939.4465](https://doi.org/10.3406/bulmi.1939.4465). URL: [https://www.persee.fr/doc/bulmi\\_0366-3248\\_1939\\_num\\_62\\_4\\_4465](https://www.persee.fr/doc/bulmi_0366-3248_1939_num_62_4_4465) (cit. on p. 8).
- [60] Max Born. “Theoretical investigations on the relation between crystal dynamics and x-ray scattering”. In: *Reports on Progress in Physics* 9.1 (1942), pp. 294–333. doi: [10.1088/0034-4885/9/1/319](https://doi.org/10.1088/0034-4885/9/1/319). URL: <https://doi.org/10.1088/0034-4885/9/1/319> (cit. on p. 8).
- [61] R W James. *The optical principles of the diffraction of x-rays*. London: G. Bell and Sons, 1948 (cit. on p. 8).
- [62] Marco Bernardi. “First-principles dynamics of electrons and phonons”. In: *The European Physical Journal B* 89.11 (2016), p. 239. ISSN: 1434-6036. doi: [10.1140/epjb/e2016-70399-4](https://doi.org/10.1140/epjb/e2016-70399-4). URL: <https://doi.org/10.1140/epjb/e2016-70399-4> (cit. on p. 9).
- [63] Matin Amani, Der-Hsien Lien, Daisuke Kiriya, Jun Xiao, Angelica Azcatl, Jiyoung Noh, Surabhi R. Madhvapathy, Rafik Addou, Santosh KC, Madan Dubey, Kyeongjae Cho, Robert M. Wallace, Si-Chen Lee, Jr-Hau He, Joel W. Ager, Xiang Zhang, Eli Yablonovitch, and Ali Javey. “Near-unity photoluminescence quantum yield in MoS<sub>2</sub>”. In: *Science* 350.6264 (2015), pp. 1065–1068. doi: [10.1126/science.aad2114](https://doi.org/10.1126/science.aad2114). eprint: <https://www.science.org/doi/pdf/10.1126/science.aad2114>. URL: <https://www.science.org/doi/abs/10.1126/science.aad2114> (cit. on p. 9).
- [64] Yiling Yu, Yifei Yu, Chao Xu, Andy Barrette, Kenan Gundogdu, and Linyou Cao. “Fundamental limits of exciton-exciton annihilation for light emission in transition metal dichalcogenide monolayers”. In: *Phys. Rev. B* 93 (20 2016), p. 201111. doi: [10.1103/PhysRevB.93.201111](https://doi.org/10.1103/PhysRevB.93.201111). URL: <https://link.aps.org/doi/10.1103/PhysRevB.93.201111> (cit. on p. 9).
- [65] Edbert J. Sie, Alex J. Frenzel, Yi-Hsien Lee, Jing Kong, and Nuh Gedik. “Intervalley biexcitons and many-body effects in monolayer MoS<sub>2</sub>”. In: *Phys. Rev. B* 92 (12 2015), p. 125417. doi: [10.1103/PhysRevB.92.125417](https://doi.org/10.1103/PhysRevB.92.125417). URL: <https://link.aps.org/doi/10.1103/PhysRevB.92.125417> (cit. on p. 12).
- [66] Li-Dong Zhao, Shih-Han Lo, Yongsheng Zhang, Hui Sun, Gangjian Tan, Ctirad Uher, C. Wolverton, Vinayak P. Dravid, and Mercouri G. Kanatzidis. “Ultralow thermal conductivity and high thermoelectric figure of merit in SnSe crystals”. In: *Nature* 508.7496 (2014), pp. 373–377. ISSN: 1476-4687. doi: [10.1038/nature13184](https://doi.org/10.1038/nature13184). URL: <https://doi.org/10.1038/nature13184> (cit. on p. 13).
- [67] Li-Dong Zhao, Cheng Chang, Gangjian Tan, and Mercouri G. Kanatzidis. “SnSe: a remarkable new thermoelectric material”. In: *Energy Environ. Sci.* 9 (10 2016), pp. 3044–3060. doi: [10.1039/C6EE01755J](https://doi.org/10.1039/C6EE01755J). URL: <http://dx.doi.org/10.1039/C6EE01755J> (cit. on p. 13).
- [68] Fabio Caruso, Maria Troppenz, Santiago Rigamonti, and Claudia Draxl. “Thermally enhanced Fröhlich coupling in SnSe”. In: *Phys. Rev. B* 99 (8 2019), p. 081104. doi: [10.1103/PhysRevB.99.081104](https://doi.org/10.1103/PhysRevB.99.081104). URL: <https://link.aps.org/doi/10.1103/PhysRevB.99.081104> (cit. on p. 13).
- [69] Weng Hong Sio, Carla Verdi, Samuel Poncé, and Feliciano Giustino. “Ab initio theory of polarons: Formalism and applications”. In: *Phys. Rev. B* 99 (23 2019), p. 235139. doi: [10.1103/PhysRevB.99.235139](https://doi.org/10.1103/PhysRevB.99.235139). URL: <https://link.aps.org/doi/10.1103/PhysRevB.99.235139> (cit. on p. 13).
- [70] Jarvist Moore Frost, Lucy D. Whalley, and Aron Walsh. “Slow Cooling of Hot Polarons in Halide Perovskite Solar Cells”. In: *ACS Energy Letters* 2.12 (2017). PMID: 29250603, pp. 2647–2652. doi: [10.1021/acsenergylett.7b00862](https://doi.org/10.1021/acsenergylett.7b00862). eprint: <https://doi.org/10.1021/acsenergylett.7b00862>. URL: <https://doi.org/10.1021/acsenergylett.7b00862> (cit. on p. 13).
- [71] Marios Zacharias and Feliciano Giustino. “Theory of the special displacement method for electronic structure calculations at finite temperature”. In: *Phys. Rev. Research* 2 (1 2020), p. 013357. doi: [10.1103/PhysRevResearch.2.013357](https://doi.org/10.1103/PhysRevResearch.2.013357). URL: <https://link.aps.org/doi/10.1103/PhysRevResearch.2.013357> (cit. on p. 13).

- [72] Wu Li, Jesús Carrete, Nabil A. Katcho, and Natalio Mingo. “ShengBTE: A solver of the Boltzmann transport equation for phonons”. In: *Computer Physics Communications* 185.6 (2014), pp. 1747–1758. ISSN: 0010-4655. DOI: <https://doi.org/10.1016/j.cpc.2014.02.015>. URL: <https://www.sciencedirect.com/science/article/pii/S0010465514000484> (cit. on p. 16).